Imperial College London

FINAL REPORT FOR MSc INDIVIDUAL PROJECT

DEPARTMENT OF BIOENGINEERING

Use of hyperspectral image analysis in neurosurgery

Author:
Victoire de Saléon-Terras

Supervisor:
Dan Elson

Submitted in partial fulfillment of the requirements for the award of MSc degree in
Biomedical Engineering of Imperial College London

September 2023
Word count : 4819 words

Abstract

Surgical resection of brain tumors is a one of the main treatment options for brain cancer, demanding precise differentiation between tumor margins and normal brain tissue. This study aims to develop a real-time surgical guidance system employing Hyperspectral Imaging (HSI) to address this clinical need. HSI exploits light-tissue interactions across diverse wavelengths, offering advantages of rapid image acquisition, non-invasiveness, high spectral and spatial resolution, and portability. The study is based on extensive research into the optical properties of biological tissues in the visible range, particularly in brain tissue.

The project focuses on processing hyperspectral data acquired during surgical resections, with specific emphasis on meningioma cases. Meningiomas are generally benign tumors originating from the meninges, the protective layers around the brain and spinal cord. Investigating whether meningiomas infiltrate the dura mater, the outermost meningeal layer, is a key objective. The estimation of blood oxygenation levels in exposed intracranial tissues, especially the dura, during surgery should provide valuable diagnostic information.

This research implements algorithms to generate oxygen saturation maps based on previously developed methods, utilizing a multi-parameter wavelength-dependent data fit. A Monte-Carlo simulation model describing light transport in biological tissues is integrated, enabling spectral data fitting and oxygen saturation map generation. Processed hyperspectral data holds promise for future tissue classification algorithms.

By utilizing HSI as an intraoperative guidance tool, this study seeks to enhance the precision and safety of brain tumor resections, aiding surgeons in preserving vital brain functions while maximizing tumor removal.

Acknowledgments

Contents

Chapter 1

Introduction

1.1 Background

1.1.1 Surgical resection of brain tumours

Surgical resection of brain tumours is one of the major treatment options for brain cancer (along with radiotherapy and chemotherapy). During this medical procedure, the surgeon must remove as much tumour tissue as possible while preserving the surrounding normal brain. However, it is challenging to identify the margins of the tumour with the naked eye as they often fade into normal brain tissue. Unlike other organs in the body, the removal of tumour tissue beyond the visible margins is limited by the presence of critical functional areas in the brain that must be preserved to avoid permanent disability. The concept of "functional margins of resection" has been established, where tumour resection is pushed up to 1-2 cm beyond the margins or up to the point where a functional area is found. Identifying these areas and the tumour tissues is the main challenge in brain tumour surgical resection.

1.1.2 Brain tissues oxygenation

The tumour progression and growth have been shown to depend on a great amount of oxygen and nutrient supply for energy production. New vascular networks are formed to meet the increased metabolic demand and to provide roads for tumour cell migration. Some studies have demonstrated that techniques including blood oxygenation level imaging and vascular architecture mapping provide valuable information on tumours (Preibisch et al. [2017]). In addition, monitoring tissue oxygenation during a neurosurgical procedure is essential as one of the important predictors of recovery and viability of the tissues relies on its oxygen supply. Finally, assessing blood oxygenation levels in the brain can provide valuable insights into brain activity and functional areas. Typically through techniques like blood-oxygen-level dependent (BOLD) functional magnetic resonance imaging (fMRI) (Rodgers et al. [2016]). But this method can only be applied before the surgery and can't be used as an intra-operative surgical guidance system.

1.2 Aim of the study

1.2.1 Imaging system for surgical guidance

There is a clinical need for a device that can better identify differences between tumour margins, normal brain tissue and functionally active areas during the neurosurgical procedure. The aim of the study is therefore to provide the surgical team with a surgical guidance system. It should be capable of imaging and processing data in real-time and displaying diagnostic data such as brain perfusion (levels of oxygenated/ deoxygenated hemoglobin).

1.2.2 Motivations for using hyperspectral imaging

Hyperspectral imaging (HSI) exploits the interaction of light and biological tissue at diverse wavelengths in the electromagnetic spectrum, with the purpose of retrieving physiological information (such as blood oxygenation levels). HSI as an intraoperative guidance tool offers several advantages. First, it has a short time of image acquisition. Secondly, it is non-invasive and non-ionising. This optical imaging technique provides high spectral and spatial resolution data. Finally, optical imaging devices are generally safe and portable, allowing easy integration into the surgical workflow. HSI has been widely used in medical research to monitor brain tissue metabolism and hemodynamics (Giannoni et al. [2018]). The optical properties of biological tissues in the visible range (450-750nm), especially brain tissue, have been extensively studied (Jacques [2013], Ali [2023]). This provides us with a wide source of documentation for developing our hyperspectral image analysis systems.

1.3 Project description

1.3.1 Processing of hyperspectral images of meningioma cases

This research project focuses on the processing of the hyperspectral data acquired during surgical resection of brain tumour. In this study, the processed images will be those of patients with meningiomas (among the 48 research participants, 10 were meningioma cases). A meningioma is a type of brain tumor that arises from the meninges, the protective layers of tissue that cover the brain and spinal cord. Meningiomas are typically slow-growing and are usually benign. However, they can cause problems if they grow large and exert pressure on nearby brain tissue or structures (cancerresearchuk.org [2023]). As this type of tumour grows outside of the brain (unlike gliomas for example), the research team wants to investigate how meningioma infiltrates the dura. The dura mater is the outermost and toughest of the three layers of the meninges that surround the brain and spinal cord. The research team's aim is to verify whether a correlation between oxygenation levels and dura infiltration can be detected by a hyperspectral camera.

1.3.2 Aim of the codes

Based on methods developed in previous studies, I implemented programs that generate oxygen saturation maps. In previous studies, several algorithms have already been

developed to determine blood oxygenation levels in biological tissues using a multi-parameter wavelength-dependent data fit (Yeganeh et al. [2012], Yin et al. [2013]). Therefore, we chose to implement a fitting procedure. First, we needed to elaborate a model that describes the light transport in biological tissues. For this purpose, a Monte-Carlo simulation has been developed. Secondly, we needed a program to fit the spectral data acquired during the surgeries to this model and to generate oxygen saturation maps. Previous studies have demonstrated that these processed hyperspectral data can then be used for tissue classification algorithms (Fabelo et al. [2019]).

Chapter 2

Methods

The flowchart Figure 2.1 summarize the study material and protocol's steps described in this chapter. During the surgeries, the surgeon a camera connected to LCTF filters (Section 2.1.1), to acquire hyperspectral images of brain tissues of the research participants and white references (Section 2.1.2). With the programs I implemented, I first corrected the spectral intensity with the spectral response of the imaging system to obtain the true spectral intensity. Then, using an absorptivity model (Section2.2) and a fitting algorithm (Section 2.3), the program estimates oxygen saturation and total hemoglobin concentration.
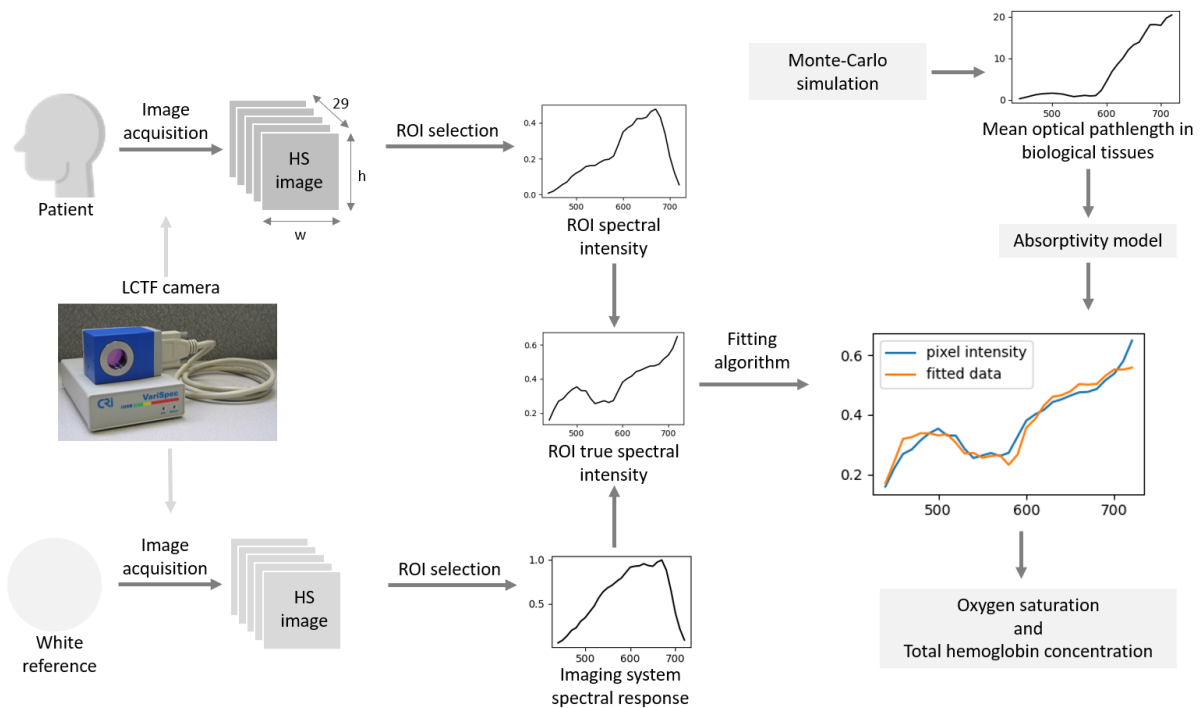

Figure 2.1: Flowchart explaining the study's protocol

2.1 Study material

2.1.1 Liquid Crystal Tuneable Filter

During the surgeries, the images were filtered through a Liquid Crystal Tunable Filter (LCTF) (Figure 2.2) so that the camera acquired images of a scene at multiple wavelengths. The wavelength was electronically controllable, providing rapid and vibrationless selection of any wavelength in the visible spectrum. The LCTF was connected to the operative microscope and endoscope during the neurosurgery. It was set to acquire images in 29 spectral bands from 440 nm to 720 nm. The transmission of the tunable filters for these 29 spectral bands is shown Figure 2.3. 48 patients undergo the surgery during which multiple images were acquired with this camera, at different stages of the tumour resection. From March 2021 to July 2022 (27 patients), a first camera with a pixel depth of 8 bits was used, and then from September 2022 to July 2023 (21 patients), it was replaced by a second camera with a pixel depth of 16 bits.
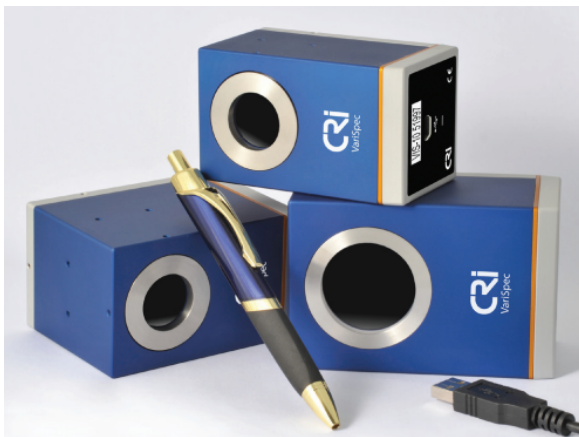

Figure 2.2: VariSpec Liquid Crystal Tunable Filters from CRI, image from the technical notes
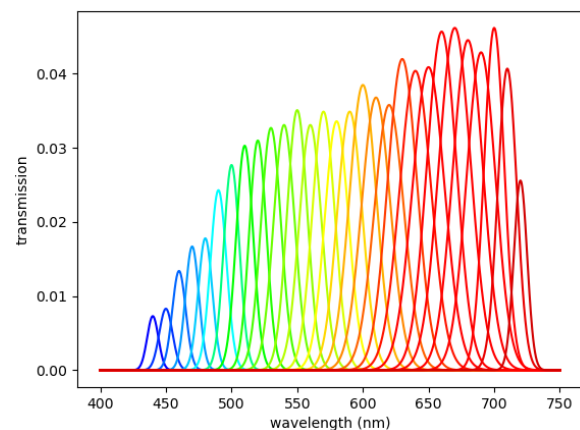

Figure 2.3: Transmission of the filters tuned at 29 different wavelengths from 440 nm to 720 nm

2.1.2 Study protocol

Recruitment of the research participants

Patients were informed of this study during their first neuro-oncology consultation. A member of the research team was present at the time of the consultation and explained in detail what are the purposes and the methods of the study. Any patient with a diagnosis of brain tumour, age ranging from 18 with no upper limit, who agreed to the operation and to take part in the study, was enrolled. Patients suspected of another pathological condition affecting the central nervous system were not included, as well as patients unwilling to take part in the present research protocol, or with a lack of capacity (patients who are not capable of understanding, processing, and retaining information). Enrolment and surgeries proceeded for 2 years (from March 2021 to August 2023). Consent was taken by a member of the research team, who is also a member of the direct care team. If the patient did agree to take part in the study, the patient signed the consent form for research within the day before surgery, thus allowing sufficient time for questions and autonomous research about the topic.

Surgical intervention and collection of spectral data

Patients who have agreed to take part in the study were admitted to Charing Cross Hospital, Neurosurgery Department. During surgery, the operating surgeon, also a member of the research team, performed the standard procedure for resection of the brain tumour, and used standard NHS neurosurgical equipment. The only technical modification is that either the microscope or the endoscope in use was connected to the system of cameras and filters for hyperspectral acquisition. The use of this imaging acquisition technique did not change standard operative practice, nor interfere with the principles of neurological surgery. During each surgical intervention, spectral data were collected at specific stages: mostly once the brain surface was exposed and at the end of resection on the surgical cavity.

Acquisition of white references

For each hyperspectral acquisition series, a white screen was also imaged to be used as a white reference. This object reflects or emits light in a known and uniform manner across the visible spectrum. Thus the images are used to determine the camera response to light. This step in the study methodology is essential for obtaining reliable and comparable measurements, as it helps eliminate potential biases and variations caused by the system's response to light. An algorithm was written to obtain the camera response spectrum from reference white images. The steps of this algorithm are summarized below:

- The program opens the white reference hyperspectral image and displays one frame

- The user clicks on one pixel with their cursor. It defines a 100×100 pixels region of interest (ROI).

- If some pixels in the ROI are saturated, the user has to find another ROI.

- The program calculates the mean spectrum of the ROI

- The program saves the mean spectrum in a new column of a .csv file, with the hyperspectral image references (patient number and run number)

- Then, an average of all the response spectrum for each camera is calculated.

2.1.3   Spectral data

The surgeon acquires images at several stages of the surgery (4 to 15 runs, including the white reference runs). The images are saved as a folder of 29 PNG or TIF images with the acquisition information (timestamp, exposure time...). Along with the different hyperspectral runs, some images are taken and then segmented by a specialist with the label of the different tissues (see Figure 2.5). Using the segmentation of the dura, tumour core, ... given by the specialist, a mask is created to isolate the tissues of interest in the hyperspectral images.
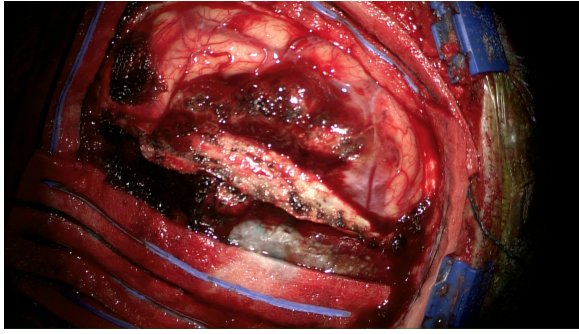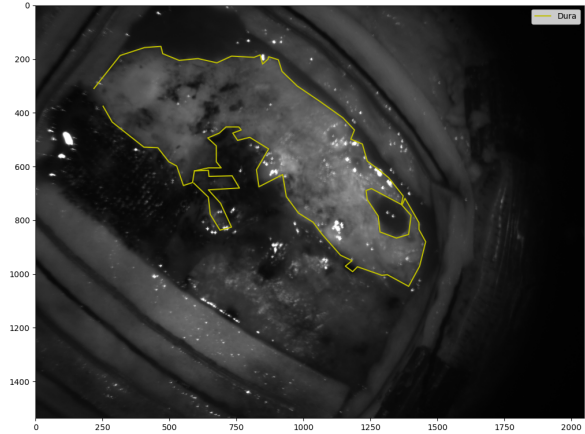
Figure 2.4: Microscope image of case HS046

Figure 2.5: Image at a wavelength of 680 nm of case HS046, run 04 with segmented dura by a specialist

2.2 Light transport in biological tissues

In this section, we aim to model light transport in biological tissues. First, we will define the various parameters characterizing optical properties of the tissues (Section 2.2.1). Then we will describe the implementation of the Monte-Carlo simulation (Section 2.2.2)

2.2.1 Optical properties of biological tissues

Light absorption and scattering are the two main phenomena occurring when light travels through biological tissues.

Absorption When light passes through biological tissues, it can be absorbed by chromophore molecules, such as hemoglobin (Jacques [2013]). Hemoglobin has different absorption characteristics depending on its oxygenation state. Hemoglobin carrying oxygen is referred to as oxyhemoglobin (HbO_2) and the deoxyhemoglobin molecule (Hb) is the form of hemoglobin without any additional molecules. These two states of hemoglobin are the major absorbing components in the brain in the visible range (400 - 800 nm). Therefore, the assessment of changes in their relative concentration is possible by measuring variations in the absorption of brain tissue. The absorption coefficient μ_a is defined as the probability of photon absorption in a medium per unit path length. It has a representative value of $0.1 cm^{-1}$ in biological tissues. According to the definition of the absorption coefficient, light attenuates as it propagates in an absorbing-only medium according to the following equation:

$$\frac{dI}{I} = -\mu_a dx \tag{2.1}$$

Where I denotes the light intensity and x denotes the distance along the light direction propagation. Integrating equation 2.1 leads to the well known Beer law:

$$I(x) = \exp(-\mu_a x) \tag{2.2}$$

The absorption of a sample is calculated as the sum of each chromophore component concentration times its molar extinction coefficient $\varepsilon(\lambda)$. Figure 2.6 shows the molar extinction coefficients of oxyhemoglobin HbO_2 and deoxyhemoglobin Hb. An example

of the absorption coefficient is represented Figure 2.7 with the black line (here, the hemoglobin concentrations are: $C_{HbO_2} = 48\mu mol.L^{-1}$ and $C_{Hb} = 12\mu mol.L^{-1}$). Once the concentrations C_{HbO_2} and C_{HbO} are known, the oxygen saturation SO_2 and the total concentration of hemoglobin C_t can be computed as follows:

$$SO_2 = \frac{C_{HbO_2}}{C_{HbO_2} + C_{Hb}}$$
$$C_t = C_{HbO_2} + C_{Hb} \tag{2.3}$$

Scattering Biological tissues contain various structures such as cells and extracellular components, which scatter light. Scattering causes the light to change its direction and propagate in multiple paths within the tissue. The extent of scattering depends on the tissue's composition, structure, and the wavelength of the incident light. The scattering coefficient μ_s is defined as the probability of photon scattering. According to Jacques [2013], the reduced scattering coefficient can be modeled as:

$$\mu'_s = a \times (\frac{\lambda}{500})^{-b} \tag{2.4}$$

with a the reduced scattering coefficient at $\lambda = 500nm$, and b a dimensionless value called "scattering power". An example of scattering coefficient is represented Figure 2.7 with the green line (here, $a = 24cm^{-1}$ and $b = 1.6$, example values from Jacques [2013])
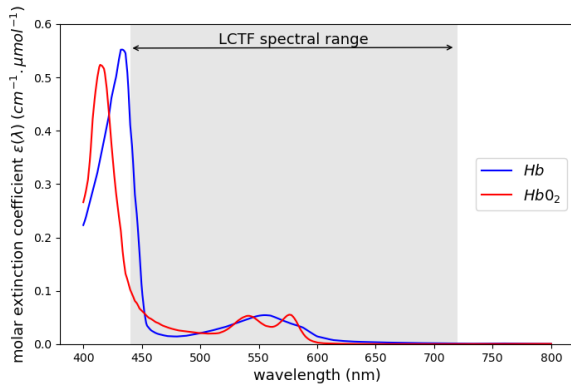

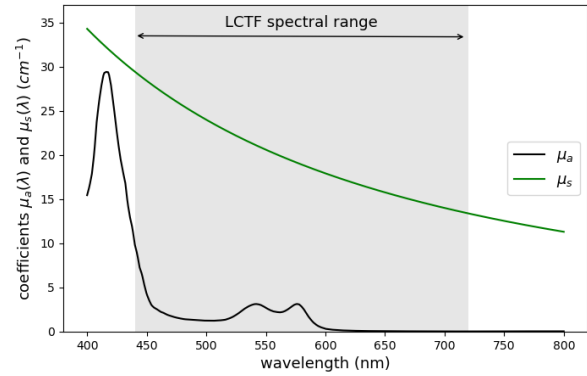**Figure 2.6:** Molar extinction coefficient of oxyhemoglobin and deoxyhemoglobin

Figure 2.7: Example of absorption coefficient and scattering coefficient

Absorptivity The Beer–Lambert law relates the absorption of light by the concentration of the components X of the biological tissue according to the following equation:

$$A(\lambda) = \mu_a(\lambda) \times x + \mu_s(\lambda) \times x$$
$$= \sum_X C_X \varepsilon_X(\lambda) \times x + \mu_s(\lambda) \times x \tag{2.5}$$

where $A(\lambda)$ is the absorptivity, or absorbance spectrum, C_X is the concentration of component X, ε_X is the molar extinction coefficient of component X, and x is the distance between the light source and the detector. The intensity spectrum acquired by the imaging system is related to the absorptivity as follows:

$$I(\lambda) = I_0 10^{-A(\lambda)}$$
$$A(\lambda) = \log_{10}(I_0) - \log_{10}(I(\lambda)) \tag{2.6}$$

Differential path length factor Depending on the optical properties of the biological components of the tissue and the wavelength λ of the light source, photons can

experience multiple scattering events. Thus, the actual optical pathlength $l(\lambda)$ is much larger than the source-to-detector separation x, and so the differential pathlength factor $DPF(\lambda)$ was incorporated into the equation 2.5 to take photon scattering into account:

$$
\begin{aligned}
A(\lambda) &= \mu_a(\lambda) \times x \times DPF(\lambda) \\
&= \sum_X C_X \varepsilon_X(\lambda) \times x \times DPF(\lambda) \\
l(\lambda) &= x \times DPF(\lambda)
\end{aligned}
\tag{2.7}
$$

The unknown values we wish to deduce using a fitting algorithm are the concentrations C_X. For this purpose, we use the model of absorptivity described above (the absorbtivity is deduced from the intensity measured by the camera using equation 2.6). But we still need to determine the optical path length $l(\lambda)$ to implement a wavelength-dependent fitting algorithm with the concentrations C_X as parameters. To achieve this, photon transport in biological tissue is numerically simulated by the Monte Carlo method in the next section.

2.2.2 Monte-carlo simulation to estimate the mean optical pathlength

Monte Carlo simulation is a computational technique. We are going to use it to model the propagation of light and estimate its behavior within the tissue, inspired by the work of Wang and i Wu [2009]. Monte Carlo simulation is based on the concept of random sampling. It involves generating a large number of random photon packet trajectories within the tissue and tracking their paths as they undergo scattering and absorption events. Each photon packet follows a random walk, with its direction determined by scattering angles and its path affected by absorption. This simulation is performed in a three-dimensional representation of the tissue, with the z axis being orthogonal to the tissue surface, and the xy plane coincides with the tissue surface.

To estimate the mean optical path length, the Monte Carlo simulation records the total distance traveled by each photon before it is reemitted back in the ambient medium. By averaging the path lengths of multiple photon packets, an estimate of the mean optical path length is obtained. The accuracy of the Monte Carlo simulation depends on several factors, including the tissue model used, the optical properties assigned to the tissue components, and the number of photons simulated. Increasing the number of simulated photons improves the accuracy of the estimation, but it also increases the computational cost.

Representation of a photon packet As described in Wang and i Wu [2009], the simulation consists of allowing a packet of photons with a weight W to propagate along a particular trajectory. The parameters of a photon packet are:

- the cartesian coordinates (x, y, z) for tracking the photon packet.

- the direction cosines of the photon packet propagation (dpx, dpy, dpz)

- the weight of the photon packet (W), that decreases as the photon packets propagates in the tissue and is being absorbed

- The distance travelled by the photon packet (D), that is updated after each step.

Initialisation For the purpose of the simulation, we model a medium in which the photon packet propagates. To mimic the properties of brain tissues we set the different parameters as follows:

- Anisotropy (g): Anisotropy refers to the directional dependence of light behavior as it interacts with and propagates through the tissue. It arises from the structural and compositional characteristics of the tissue (biological tissues often have complex microstructures, such as fibers, cells, or membranes), which can vary in different directions. It has a value between -1 and 1. A value of zero indicates isotropic scattering, and a value close to unity indicates dominantly forward scattering. For most biological tissues $g \simeq 0.9$ (Wang and i Wu [2009]).

- Mediums refractive indexes (n_0 for the ambient medium and n_1 for the tissue): The refractive index of a medium is a measure of how much light or other electromagnetic waves slow down and bend when they pass through that medium compared to their speed in a vacuum. We set $n_0 = 1.00$ (air) and $n_1 = 1.40$.

- Critical angle (α_c): The critical angle of an interface is the angle of incidence at which a light ray, traveling from a denser medium to a less dense medium, results in total internal reflection rather than refraction ($sin(\alpha_c) = n_0/n_1$).

One photon packet at a time is launched orthogonally onto the scattering medium. Each new photon packet is initialised as fallows:

- The cartesian coordinates are set to $(0, 0, 0)$

- The direction cosines of the photon packet propagation are set to $(0, 0, -1)$, as they initially propagate along the z axis.

- The weight $W = 1 - R_{sp}$ with $R_{sp} = \frac{(n_0 - n_1)^2}{(n_0 + n_1)^2}$ the specular reflectance at the first interface

Random step Each iteration the photon packet moves towards the direction (dpx, dpy, dpz) and with a step size of s_i. The step size s_i is sampled using the following sampling equation:

$$s_i = -\frac{ln(\xi)}{\mu_t} \tag{2.8}$$

With ξ a random variable uniformly distributed and $\mu_t = \mu_a + \mu_s$ the extinction coefficient. This formula is directly derived from equation 2.1, and the calculations to achieve this are described in Wang and i Wu [2009].

Movement of a photon packet Once the step s_i is determined, the photon packet is moved. The coordinates of the photon packet are updated:

$$\begin{aligned}
x_{i+1} &= x_i + dpx_i \times s_i \\
y_{i+1} &= y_i + dpy_i \times s_i \\
z_{i+1} &= z_i + dpz_i \times s_i
\end{aligned} \tag{2.9}$$

Each step, the photon packet undergoes absorption and scattering. A fraction of the weight (ΔW) is absorbed :

$$\Delta W = \frac{\mu_a}{\mu_s} W$$
$$W_{i+1} = W_i - \Delta W \tag{2.10}$$

For scattering, as calculated by Wang and i Wu [2009], the new propagation direction of the photon packet can be represented as:

$$dpx_{i+1} = \frac{\sin(\theta)(dpx_i dpz_i - dpy_i \sin(\phi))}{\sqrt{1 - dpz_i^2}} + dpx_i \cos(\theta)$$
$$dpy_{i+1} = \frac{\sin(\theta)(dpy_i dpz_i - dpx_i \sin(\phi))}{\sqrt{1 - dpz_i^2}} + dpy_i \cos(\theta) \tag{2.11}$$
$$dpz_{i+1} = \sqrt{1 - dpz_i^2} \sin(\theta) \cos(\phi) + dpz_i \cos(\theta)$$

If the photon direction is sufficiently close to the z axis (e.g. $|dpz_i| > 0.999999$), the following formulas are used instead so that division by a small number is avoided:

$$dpx_{i+1} = \sin(\theta) \cos(\phi)$$
$$dpy_{i+1} = \sin(\theta) \sin(\phi) \tag{2.12}$$
$$dpz_{i+1} = sgn(dpz_i) \cos(\theta)$$

Where $sgn(.)$ is the sign function (returns 1 when dpz_i is positive and -1 when dpz_i is negative). The azimuthal angle ϕ, which is assumed to be uniformly distributed over interval $[0, 2\pi[$, is sampled with another independent random number ξ, thus $\phi = 2\pi\xi$.

Boundary crossing of a photon packet During a step, the photon packet may hit a boundary. Several steps are involved in boundary crossing. First, the distance d_b between the current location (x_i, y_i, z_i) of the photon packet and the boundary of the current layer is computed by:

$$d_b = \begin{cases} \frac{z_0 - z}{dpz} & \text{if } dpz_i < 0 \\ \inf & \text{if } dpz = 0 \\ \frac{z_0 - z}{dpz} & \text{otherwise} \end{cases} \tag{2.13}$$

Where z_0 is the boundary of the layer. Then,

- if $d_b \mu_t >= s_i$, the photon packet doesn't reach the boundary.

- if $d_b \mu_t <= s_i$, the photon packet is moved to the boundary and s is updated to $s - d_b \mu_t$.

  The angles of incidence and transmission are first calculated by:

$$\alpha_I = \cos^{-1}(|dpz|)$$
$$n_I \sin(\alpha_I) = n_T \cos(\alpha_T) \tag{2.14}$$

  if $\alpha_i > \alpha_c$, the photon packet is totally reflected

  if $\alpha_i <= \alpha_c$, the photon packet is transmitted

Since the only boundary in this simulation is the interface between the tissue and the ambient medium, when the photon packet crosses this boundary, no further step is sampled.

Termination of a photon packet A photon packet can be terminated by reemission in the ambient medium (as discussed above) or from absorption in the tissue. After termination, its path length is saved and then a new photon can be launched.

By averaging a large number of path lengths obtained using this process in the same conditions (same wavelength, tissue composition...) we obtain the mean optical path length for a given set of parameters. Then, to elaborate our model of absorptivity $A(\lambda)$, as described in equation 2.7, we run the simulation for multiple wavelengths in the visible range and smooth the data using a convolution function so that we obtain $l(\lambda)$. We now have all the necessary data for the fitting algorithm implementation.

2.3 Model fitting

Model fitting is a type of optimization that finds an optimal set of parameters for a defined function, that best fits a given set of observations. The `curve_fit` function in Python, which is part of the `scipy.optimize` module, uses a least squares method to fit a curve to a set of data points. The least squares method is a common optimization technique used in curve fitting. The basic idea is to find the curve's parameters that minimize the sum of the squares of the differences between the observed data points and the corresponding values predicted by the curve. Mathematically, it involves minimizing the sum of the squares of the residuals, where residuals are the differences between the observed data points and the values predicted by the curve. Here, the fitting algorithm finds the optimal C_{HbO_2} and C_{Hb} for the function below, that best fits each pixel spectra.

$$I_{C_{HbO_2},C_{Hb}}(\lambda) = I_0 10^{-(C_{HbO_2}\varepsilon_{HbO_2}(\lambda)+C_{Hb}\varepsilon_{Hb})\times l(\lambda)} \tag{2.15}$$

The value of I_0 is also unknown and set as a parameter to determine during the fitting process. In the first algorithm developed, an image of the brain tissue is displayed (as in figure 2.5). The user can click on any pixel and the fitting process is done on this specific pixel's spectrum. The second algorithm developed reduces the spatial resolution of the hyperspectral image by averaging the pixels by blocs of 25×25, 40×40, ... Then the fitting process is done on every averaged spectrum of the blocs, thus creating maps of oxygenation saturation.

Chapter 3

Results

3.1 Spectral responses

The normalised spectral responses shown in Figure 3.1 were obtained using the white reference acquisitions and following the protocol described in section 2.1.2. As explained in Section 2.1.1, two cameras with different pixel depths have been used during the study, so the two spectral responses are represented below. All the spectra have also been averaged (blue line).

The spectral response algorithm has been used on all the white references available (even those from the non-meningioma cases), as we wanted the averaged spectral response to be as precise as possible. However, some spectra may not appear in Figure 3.1, as for some operations, the surgeon didn't acquire the white reference, or in some cases, the image was saturated. These spectral responses are used before the fitting process to correct the measured intensity.

The sensitivity of the optical system falls below 20% of its maximum for the shorter wavelengths ($< 470nm$) and the longer wavelengths ($> 700nm$). A lower sensitivity of the optical system may result in noisier measurements, which can affect the accuracy of the fitting algorithm's results.
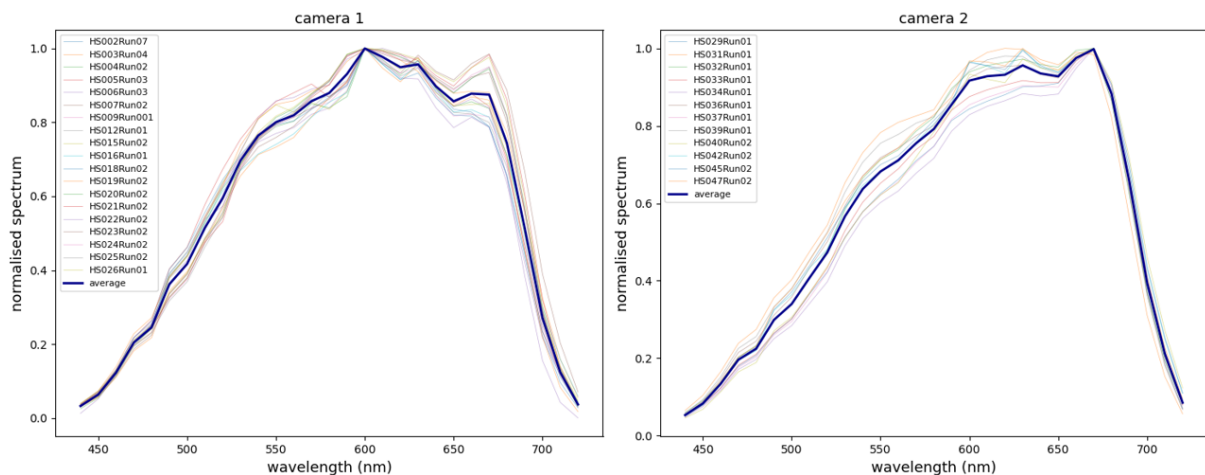
Figure 3.1: Spectral response of the imaging system using camera 1 (left) and camera 2 (right)

3.2   Mean optical path length

In this section, we present the results of the Monte-Carlo simulation aiming to estimate the mean optical path length of light in biological tissues.
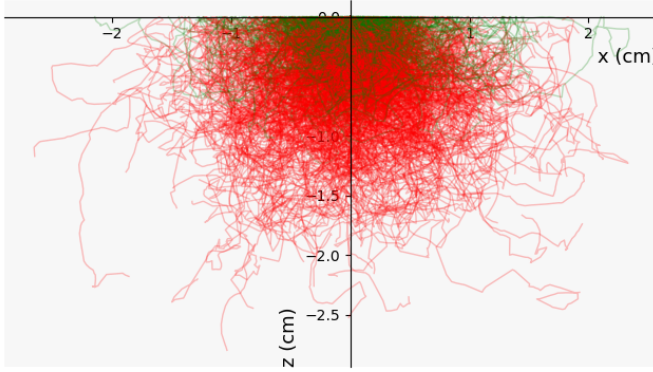
3.2.1   Random walk of photon packets

Figure 3.2: Random walk of N photon packets of wavelength 500 nm in a modelled biological tissue
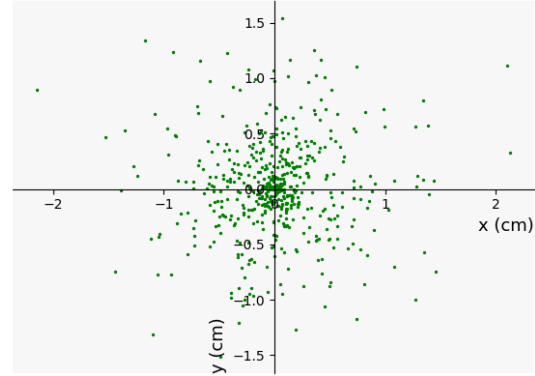

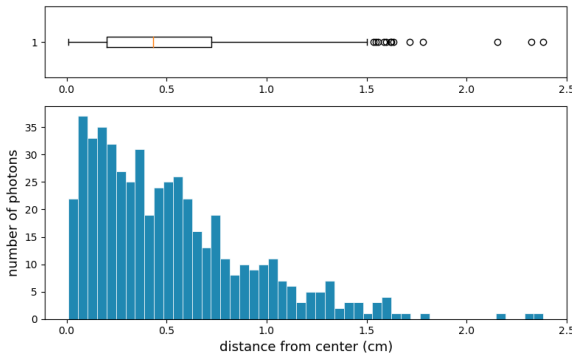**Figure 3.3:** Position of the photon packets on the tissue surface, when they are reemitted

Figure 3.4: Histogram and boxplot of the distance from the emission point and the reemission position of the photons packets
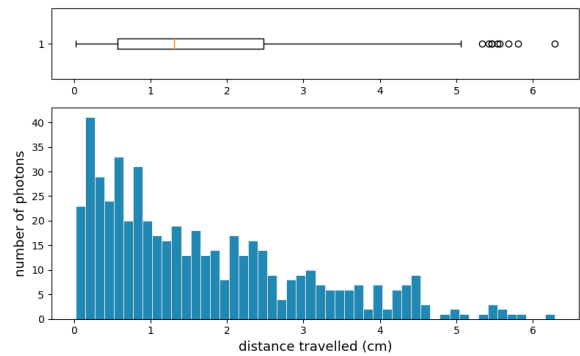
Figure 3.5: Histogram and boxplot of the distance travelled by the photon packets that have been reemitted back to the ambient medium

As described in Section 2.2.2, photon packets have been launched one after the other at the point $(x = 0, y = 0, z = 0)$. Figures 3.2 to 3.5 are the results of the launching of 1000 photon packets of wavelength $500nm$. The parameters of the modelled tissue have been set to: $g = 0.8$ (anisotropy), $C_t = 60\mu mol/L$, $SO_2 = 80\%$, $a = 24cm^{-1}$, $b = 1.6$. These parameters corresponds to the usual parameters for brain tissues according to Jacques [2013].

Figure 3.2, is a projection in the plane $(x, y = 0, z)$ of the trajectory of the 1000 photon packets. If the photon packet is transmitted back to the ambient medium it is plotted in green, and if it is absorbed in the tissue, it is plotted in red. The aspect of the photon trajectories seems plausible and similar to the results of other studies (Chatterjee et al. [2020], Polimeni et al. [2005]). The maximum penetration depth is $2.5cm$ but the photons that are reemitted don't penetrate more than $1.0cm$ into the tissue.

Among the 1000 photon packets launched, only 534 are transmitted back to the ambient medium. Figure 3.3 is the position of those 534 photons transmitted back to the ambient medium in the plane $(x, y, z = 0)$. The position of reemission of the photon packets is centered around the launching point. The distribution of the distance from this point is represented in Figure 3.4. The mean distance from the launching point is $0.45cm$.

The distribution of distances traveled by the photon packets that have been reemitted is represented in Figure 3.5. The average distance traveled is $1.3cm$ for photon packets. This value corresponds to the mean optical path length for a specific set of parameters described before. Lookup tables can then be generated by launching photon packets at multiple wavelength and for different tissue compositions

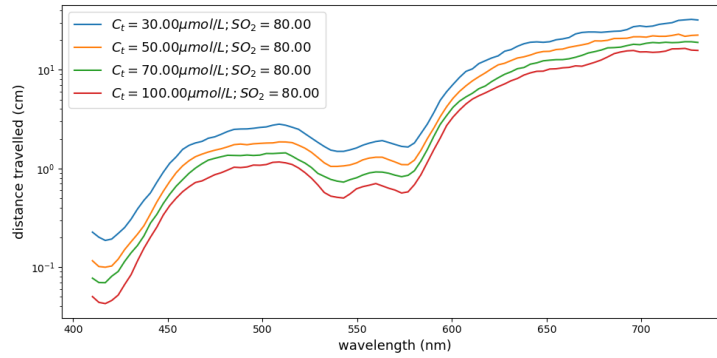### 3.2.2 Results of Monte-Carlo simulations

Figure 3.6: Comparison of different total hemoglobin concentration on the mean optical pathlength

Arrays of mean optical path length $l(\lambda)$ have been generated for wavelengths between 400 and 800 nm. The Monte-Carlo simulation have been ran at 500 different wavelengths and for different tissue compositions. Figure 3.6 shows the influence of total hemoglobin concentration C_t on differential path length factor. The lower the total hemoglobin concentration is, the less absorbed the photons packets are, and the longer distance they can travel.

The shorter wavelengths have a mean optical path length of $0.1cm$. This value is consistent with the usual mean optical path length that we could find in the literature. But the longer wavelengths obtained are about $10cm$, above usual values for a mean optical path length. Perhaps, for the longer wavelengths, as light is closer to the Near Infra Red, other chromophores need to be taken into account, such as water.

3.3 Model fitting

3.3.1 Results simple curve fitting algorithm

The first fitting program that has been implemented asks the user to click on a pixel of the image. The fitting algorithm is then run on the spectrum of this pixel. It estimates

the best value for the parameters C_{HbO_2}, C_{Hb} and I_0 and then calculates the value of SO_2 and C_t. Figure 3.8 shows the result of the first fitting algorithm for the selected pixel Figure 3.7. The model seems to be accurate as the pixel intensity and the fitted data overlap well.
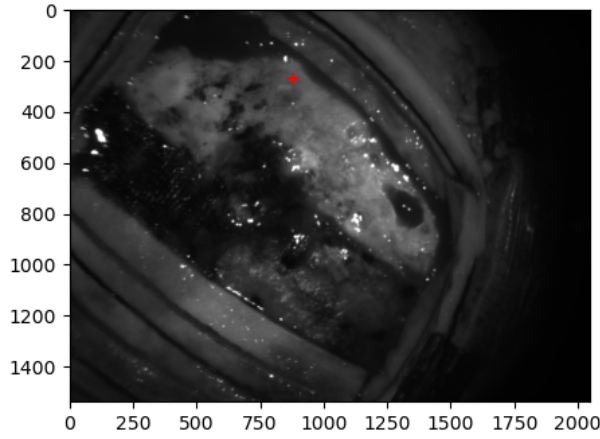

Figure 3.7: Image at a wavelength of 680 for case HS046, run 04. The red cross indicates where the user clicked
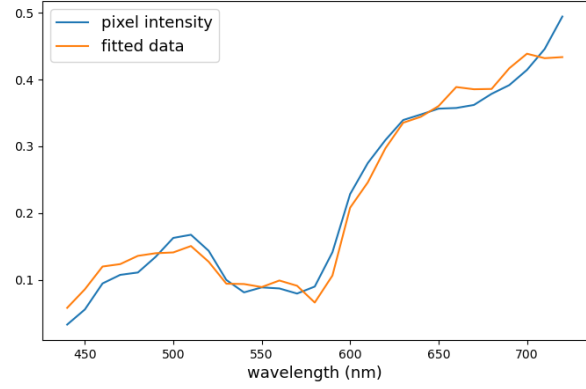

Figure 3.8: Result of the first fitting algorithm : $SO_2 = 0.76$, $C_t = 21.0\mu mol/L$, $I_0 = 0.79$

3.3.2 Oxygen levels mapping

The second fitting program that has been implemented generates oxygen saturation maps and total hemoglobin concentration maps. The pixels of the Region of Interest are averaged by blocs and the fitting algorithm is run on each of the blocs. For example, the following maps (Figure 3.9 and Figure 3.10) have been generated for the segmented dura of patient HS0046 (see Figure 2.5), and the pixels have been averaged by blocs of 25×25 pixels.
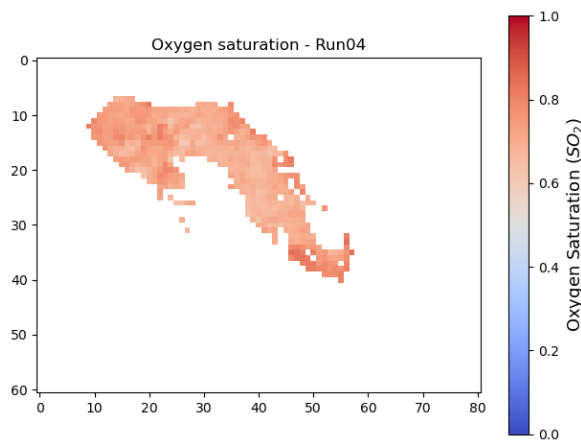

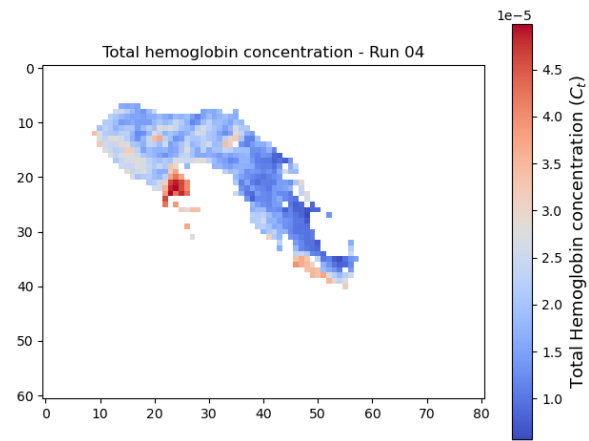**Figure 3.9:** Oxygen saturation map for case HS046, run 04

Figure 3.10: Total hemoglobin concentration map for case HS046, run 04

The program have also been tried on other images, and larger areas, including different tissues. Figure 3.11 shows the segmented tissues of HS033. A polygon have been selected manually including blood vessels, cortical surface and the tumour core. Figure 3.13 shows that the oxygen saturation is the highest in the cortical surface and the

lowest in the blood vessels. Figure 3.14 shows that the total hemoglobin concentration is the highest in the blood vessels and the lowest in the cortical surface. Figure 3.12 represents for each pixel bloc the total hemoglobin concentration plotted against the oxygen saturation. We observe different groups of locations corresponding to the different tissue types, it can then be used in SVM algorithms to classify the tissues.
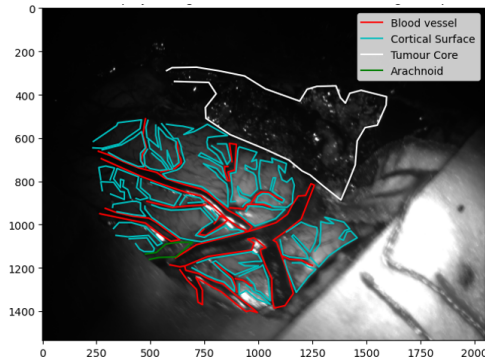

Figure 3.11: Image at a wavelength of 680 nm for case HS033, Run 05 with the labels of segmented tissues
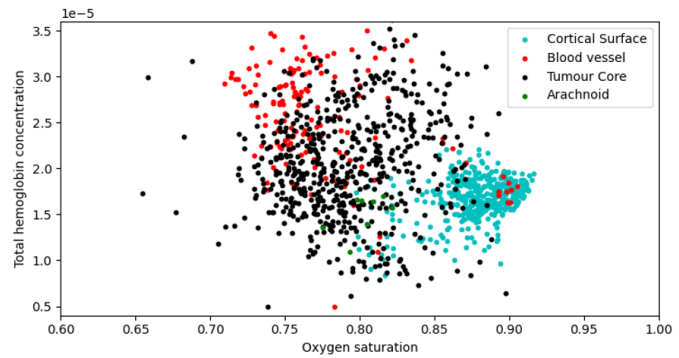

Figure 3.12: For each pixel bloc, the total hemoglobin concentration is plotted against the oxygen saturation
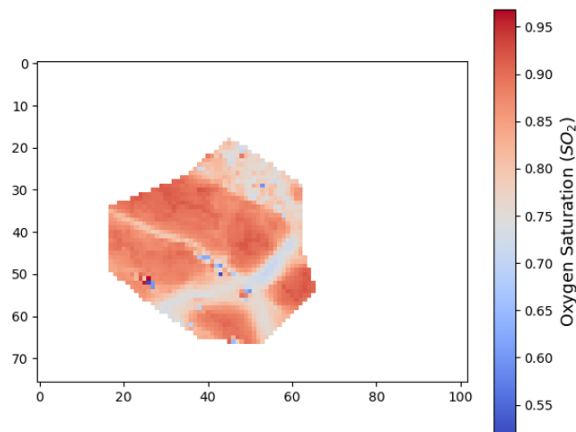

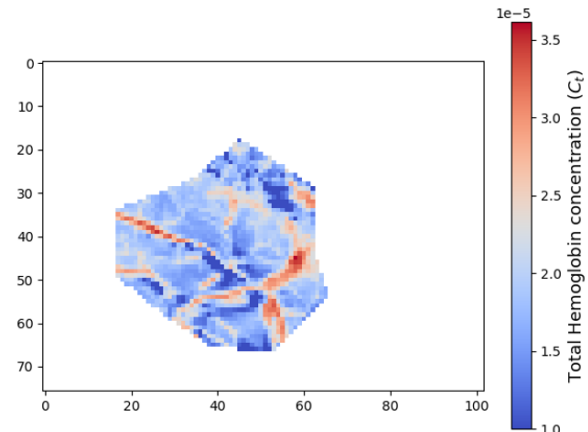**Figure 3.13:** Oxygen saturation map of case HSO33, run 05

Figure 3.14: Total hemoglobin concentration map of case HS033, run 05

As part of a separate study, I was asked to run my programs on other hyperspectral images, including non meningioma cases. The aim was to see if any change in blood oxygenation levels could be detected during the surgery if the patient was performing a task. The results are presented in the Appendix.

Chapter 4

Discussion

4.1 Clinical insight

For now, the knowledge about oxygen saturation during brain surgery is limited. The assessment of oxygen saturation with hyperspectral imaging in real-time is only at the research stage.

It isn't possible to check whether the results on blood oxygenation levels are accurate, since we don't have any comparative values. We can only verify whether the value range is of the right order of magnitude. Connective tissues' oxygen saturation levels are not precisely known, but it is common knowledge that there is a large variation between different districts, and that the perfusion is lower when compared to more constantly oxygenated tissues such as the heart, the brain, and the lungs. Therefore, meninges, including dura, are expected to have a comparatively lower saturating than the brain, especially during surgery. The blood vessels analyzed during the study are veins, so they are expected to be less oxygenated than arteries.

A good way to assess the accuracy of the optical imaging system and the data processing programs that have been developed, would be to test them on phantoms, where the concentration of their components is known. Some previous studies faced the same lack of a calibration standard and proposed tissue phantoms for quantitative calibration and performance evaluation of their spectral imaging devices (Xu et al. [2012]).

Another area to explore is the classification of tissues based on their composition, as some studies proved that classification of tissues for assistance in tumour resection is possible using deep learning (Fabelo et al. [2019]). The results of Section 3.3.2 show the possibility of using the estimated blood oxygenation levels in SVM algorithms to classify the tissues.

4.2 Calculation time

An important aspect of this study was to be able to develop a program capable of analyzing the hyperspectral data in a very short amount of time, so that the surgical team could use it during the operation. For this purpose, the codes have been written to optimize calculations and avoid unnecessary repetition.

Firstly, the program estimates the mean optical path length using Monte-Carlo simulations in approximately 2 minutes. But the calculation doesn't have to be done during the surgery and provides lookup tables for the next part of the program.

Secondly, the oxygen saturation maps and total hemoglobin concentration maps are obtained in approximately 5 minutes. However, the calculations were carried out on my personal laptop. Better times can be obtained with a computer with better performances, and also by parallelizing the calculations.

Chapter 5

Conclusion

In summary, our study aims to provide neurosurgeons with a valuable tool that can enhance the precision and safety of brain tumor resections. The ability to estimate blood oxygenation levels in various exposed brain tissues, particularly the dura, holds significant clinical relevance. Therefore, multiple programs have been implemented to generate oxygen saturation maps and total hemoglobin concentration maps.

To achieve this, we implemented multi-parameter wavelength-dependent data fitting algorithms, integrating a model of light transport in biological tissues simulated with Monte-Carlo method. The extensive documentation on the optical properties of biological tissues, especially brain tissue, provided a robust foundation for the development of these programs. The code is functional and usable by the rest of the research team.

While challenges persist, including the need for comparative data and further optimization, our study shows the potential of HSI as a valuable tool for enhancing surgical precision and patient outcomes. This study could lead to a better understanding of blood oxygenation levels during brain surgery. The methods developed can also be used to help classify the different tissues.
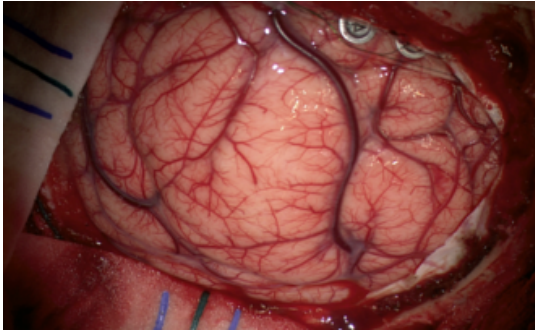
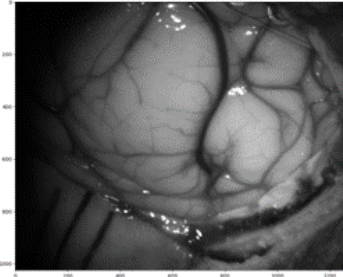# Appendix

Figure 1: Microscope image of case HS009

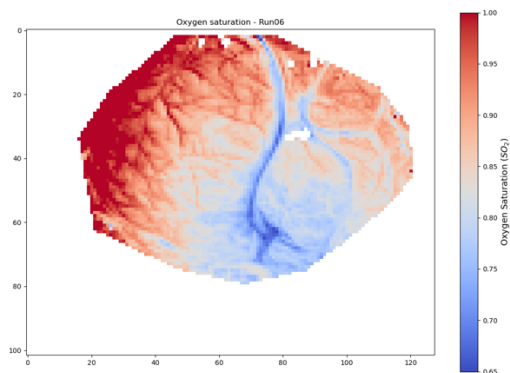**Figure 2:** Image at wavelength 680 nm of case HS009, run 06

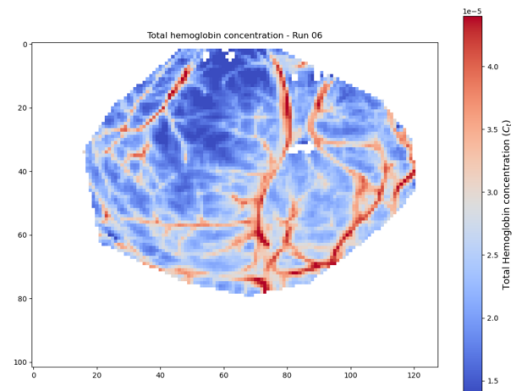**Figure 3:** Oxygen saturation map of run 06 (no task)

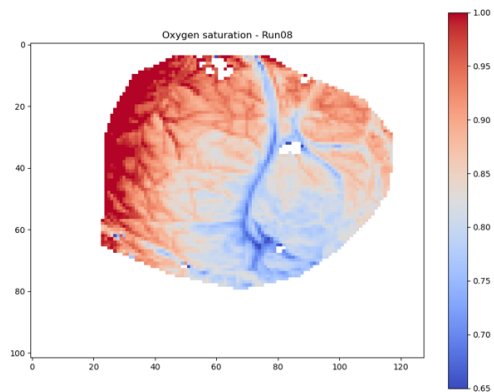**Figure 4:** Total hemoglobin concentration map of run 06

Figure 5: Oxygen saturation map of run 08 (executing task : reading)
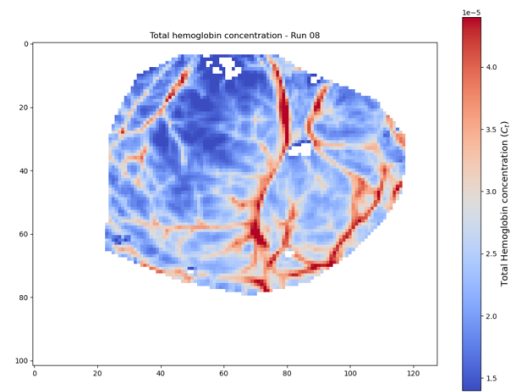

Figure 6: Total hemoglobin concentration map of run 08

Bibliography

Christine Preibisch, Kuangyu Shi, Anne Kluge, Mathias Lukas, Benedikt Wiestler, Jens Göttler, Jens Gempt, Florian Ringel, Mohamed Al Jaberi, Jürgen Schlegel, Bernhard Meyer, Claus Zimmer, Thomas Pyka, and Stefan Förster. Characterizing hypoxia in human glioma: A simultaneous multimodal mri and pet study. *NMR in Biomedicine*, 2017. URL https://doi.org/10.1002/nbm.3775. 1

Zachchary B Rodgers, John A Detre, and Felix W Wehrli. Mri-based methods for quantification of the cerebral metabolic rate of oxygen. *J Cereb Blood Flow Metab*, 36(7): 1165–85, 2016. URL https://doi.org/10.1177/0271678X16643090. 1

Luca Giannoni, Frédéric Lange, and Ilias Tachtsidis. Hyperspectral imaging solutions for brain tissue metabolic and hemodynamic monitoring: past, current and future developments. *Journal of Optics*, 2018. URL https://doi.org/10.1088/2040-8986/aab3a6. 2

Steven L. Jacques. Optical properties of biological tissues: a review. *Physics in Medicine and Biology*, 2013. URL http://dx.doi.org/10.1088/0031-9155/58/11/R37. 2, 7, 8, 14

Jamal H. Ali. Spectral optical properties of gray matter in human male brain tissue measured at 400-1100 nm. *Optics*, 2023. URL https://doi.org/10.3390/opt4010001. 2

cancerresearchuk.org. Meningioma, 2023. URL https://www.cancerresearchuk.org/about-cancer/brain-tumours/types/meningioma. 2

Hadi Zabihi Yeganeh, Vladislav Toronov, Jonathan T. Elliott, Mamadou Diop, Ting-Yim Lee, , and Keith St. Lawrence. Broadband continuous-wave technique to measure baseline values and changes in the tissue chromophore concentrations. *Biomedical Optics*, 2012. URL https://doi.org/10.1364/BOE.3.002761. 3

Cui Yin, Fangyuan Zhou, Yaru Wang, Weihua Luo, Qingming Luo, and Pengcheng Li. Simultaneous detection of hemodynamics, mitochondrial metabolism and light scattering changes during cortical spreading depression in rats based on multi-spectral optical imaging. *NeuroImage*, 2013. URL https://doi.org/10.1016/j.neuroimage.2013.02.079. 3

Himar Fabelo, Martin Halicek, Samuel Ortega, Maysam Shahedi, Adam Szolna, Juan F. Piñeiro, Coralia Sosa, Aruma J. O'Shanahan, Sara Bisshopp, Carlos Espino, Mariano Márquez, María Hernández, David Carrera, Jesús Morera, Gustavo M. Callico, Roberto Sarmiento, and Baowei Fei. Deep learning-based framework for in vivo identification of glioblastoma tumor using hyperspectral images of human brain. *Sensors*, 19(4):920, 2019. URL https://doi.org/10.3390/s19040920. 3, 18

Lihong V. Wang and Hsin i Wu. *Biomedical Optics, principles and imaging*. John Wiley and Sons, Inc., 2009. URL https://onlinelibrary-wiley-com.iclibezp1.cc.ic.ac.uk/doi/book/10.1002/9780470177013. 9, 10, 11

Subhasri Chatterjee, Karthik Budidha, and Panayiotis A Kyriacou. Investigating the origin of photoplethysmography using a multiwavelength monte carlo model. *Physiological Measurement*, 2020. URL https://doi.org/10.1088/1361-6579/aba008. 14

Jonathan R. Polimeni, Domhnull Granquist-Fraser†, Richard J. Wood, and Eric L. Schwartz. Physical limits to spatial resolution of optical recording: Clarifying the spatial structure of cortical hypercolumns. *Proceedings of the National Academy of Sciences*, 2005. URL https://doi.org/10.1073/pnas.0500291102. 14

Ronald X. Xu, David W. Allen, Jiwei Huang, Surya Gnyawali, James Melvin, Haytham Elgharably, Gayle Gordillo, Kun Huang, Valerie Bergdall, Maritoni Litorja, Joseph P. Rice, Jeeseong Hwang, and Chandan K. Sen. Developing digital tissue phantoms for hyperspectral imaging of ischemic wounds. *Biomedical Optics*, 2012. URL https://doi.org/10.1364/BOE.3.001433. 18